Nanoscale

Accepted Manuscript

This article can be cited before page numbers have been issued, to do this please use: V. Brusar, A. Senki, P. Ivatovi, J. Sancho-Parramon, P. Seleš, J. Zhang, Y. Wan, P. Yang, N. Vujicic and S. Vdovi, *Nanoscale*, 2026, DOI: 10.1039/D6NR00537C.

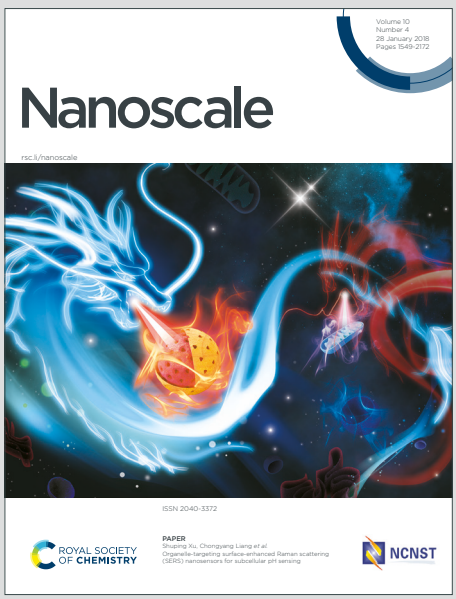

ROYAL SOCIETY OF CHEMISTRY

rsc.li/nanoscale

View Article Online
DOI: 10.1039/D6NR00537C

ARTICLE

Ultrafast and Steady-State Optical Characterization of Multilayer PdS_2

Received 00th January 20xx,
Accepted 00th January 20xx

DOI: 10.1039/x0xx00000x

Vedran Brusar,[a,b] Ana Senkić,[a,c] Petra Ivatović,[b] Jordi Sancho-Parramon,[d] Patrick Seleš,[a] Jisheng Zhang,[e] Yanfen Wan,[e] Peng Yang,[e] Nataša Vujičić [a] and Silvije Vdović *[a]

Palladium disulfide (PdS_2), a noble-metal transition metal dichalcogenide with an unusual puckered orthorhombic structure, is of interest for fundamental research and optoelectronic applications due to its distinctive optical properties. Despite this potential, PdS_2 itself remains relatively underexplored. Here, we characterize the steady-state and ultrafast optical properties of multilayer PdS_2 film using polarization-dependent Raman and second-harmonic generation microscopy, ellipsometry, and ultrafast differential reflectance. We extract the dielectric function, an indirect bandgap of 1.25 eV and confirm the 2O phase. Ultrafast measurements reveal multi-timescale dynamics, including a two-step decay (370 fs and 1.1 ps) and blueshift during photoinduced carrier relaxation, as well as coherent phonon oscillations of the A_g^1 optical mode. Long-lived carrier recombination is described by a biexponential decay with time constants of 240 ps and 2 ns. These results provide insight into the ultrafast dynamics and optoelectronic properties of PdS_2, and may open new possibilities for its use in photonic and optoelectronic devices.

Introduction

Two-dimensional (2D) transition metal dichalcogenides (TMDs) exhibit remarkable optical and electronic behaviors, including tunable bandgaps and strong light–matter interactions, making them ideal platforms for next-generation devices.[1–5] Despite extensive research on conventional TMDs, noble-metal TMDs remain a comparatively underexplored subset, even though they exhibit distinctive properties. Notably, $PdSe_2$ and PdS_2 are structurally different from other TMDs. They adopt a highly anisotropic orthorhombic layered structure built from the puckered pentagonal tiling, also known as the 2O phase or PdS_2-type structure.[6–9] The crystal structure of orthorhombic PdS_2 is shown in Fig. 1. For PdS_2, first-principles calculations predict an indirect monolayer bandgap ranging from 1.0 to 1.6 eV, which can be tuned by varying the number of layers and applying strain.[9–13] Experimental measurements on bulk PdS_2 report a bandgap of about 0.7 eV.[14] Theoretical studies also suggest several monolayer functionalities, including chemical sensing,[15] ferroelastic behavior,[16] and catalytic activity in the hydrogen evolution reaction.[17] However, this potential remains unrealized since monolayer synthesis has not yet been achieved.

Experimentally, PdS_2 has already demonstrated promising functional behavior. PdS_2 films have been used to fabricate field-effect transistors,[18] as well as broadband photodetectors, showing high carrier mobility and strong photoresponse.[19] Few-layer nanosheets have served as saturable absorbers, enabling doubly Q-switched and mode-locked optical parametric oscillation,[20] and have also been used in ultrafast fiber lasers and passive photonic devices.[21,22] In addition to these optoelectronic applications, PdS_2 nanostructures have shown promise in electrocatalysis: nanoplates with surface sulfates have facilitated efficient nitrate synthesis,[23] and nanoclusters decorating one-dimensional hollow carbon have enabled stable hydrogen evolution reaction.[24]

Although PdS_2 has attracted growing interest for its electronic and optical functionalities, its optical properties remain insufficiently characterized. Theoretical studies have addressed its band structure, strain tunability, and defect-mediated effects,[13] yet experimental insight into optical anisotropy, dielectric response, and carrier and phonon dynamics is lacking. In particular, ultrafast measurements, which are essential for probing nonequilibrium processes such as sub-picosecond carrier relaxation, bandgap renormalization (BGR), coherent phonon (CP) generation, and defect-assisted recombination, seen in related noble-metal TMDs,[25–30] have not yet been performed for PdS_2. Given this absence and the promising optoelectronic potential of PdS_2, applying ultrafast techniques could provide valuable insight into its optical dynamics.

In this work, we present an extensive experimental investigation of both the steady-state and ultrafast optical properties of centimeter-scale multilayer PdS_2 synthesized by the combination of physical vapor deposition (PVD) and

[a] Center for Advanced Laser Techniques, Institute of Physics, Bijenička 46, 10000 Zagreb, Croatia. E-mail: silvije@ifs.hr
[b] Department of Physics, Faculty of Science, University of Zagreb, Zagreb, Croatia
[c] Institute of Physics, University of Münster, Wilhelm Klemm str. 10, 48149 Münster, Germany
[d] Ruđer Bošković Institute, Bijenička cesta 54, 10000 Zagreb, Croatia
[e] National Center for International Joint Research of Photoelectric Energy Materials and Application, School of Materials and Energy, Yunnan University, Kunming 650091, P. R. China

View Article Online
DOI: 10.1039/D6NR00537C

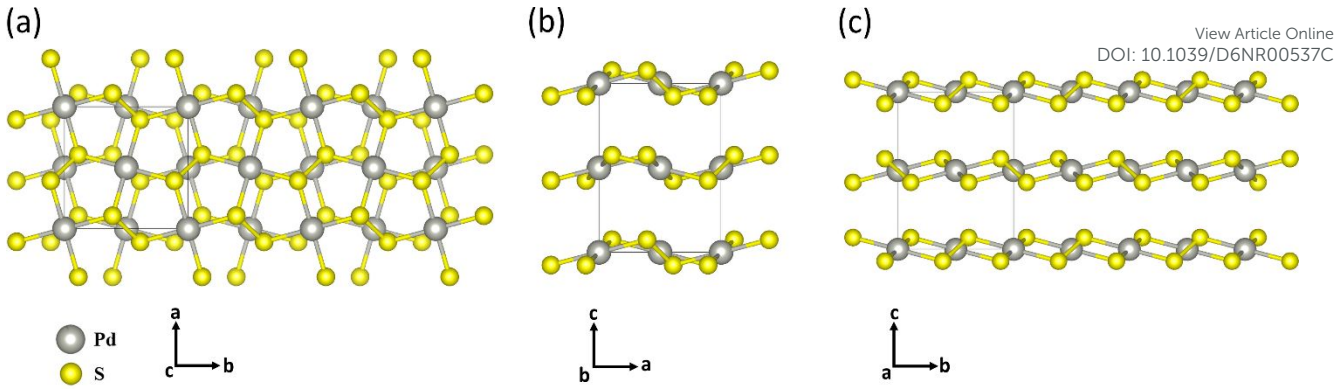

Fig. 1 Crystal structure of orthorhombic PdS_2 showing (a) top view, (b) side view along the *b*-axis, and (c) side view along the *a*-axis. The thin lines indicate the projected unit cell.

chemical vapor deposition (CVD) methods.[18] Spectroscopic ellipsometry (SE) was employed to extract the complex dielectric function, while polarization-resolved Raman and second-harmonic generation (SHG) measurements confirmed the crystal symmetry and anisotropy. Atomic-force microscopy (AFM) and energy-dispersive X-ray spectroscopy (EDS) provided complementary insights into surface morphology and stoichiometry. Ultrafast broadband differential reflectance (DR) measurements were used to probe photoinduced carrier dynamics and CP response. Together, these results provide a comprehensive picture of the steady-state and ultrafast properties of PdS_2, linking its equilibrium optical response to its nonequilibrium carrier and phonon dynamics. To the best of our knowledge, this work represents the first report of ellipsometry, SHG, and ultrafast transient spectroscopy measurements on multilayer PdS_2.

Experimental

Materials and synthesis method

The centimeter-scale multilayer PdS_2 was synthesized by combining PVD and CVD methods.[18] First, a 1×1 cm^2 silicon (Si) substrate was pre-treated by ultrasonic cleaning in deionized water, acetone, and alcohol to remove surface impurities, then dried under a nitrogen flow. A Pd film was subsequently sputtered onto the native oxidized Si surface. The Pd film was then sulfurized by placing it together with 50 mg of sulfur powder in a custom-made quartz ampoule and sealing it under a 3×10^{-4} Pa vacuum. The sealed ampoule was then placed in a horizontal tube furnace and heated to 450 °C for two hours to facilitate the sulfurization. After the reaction, the ampoule was allowed to cool naturally to room temperature.

Atomic force microscopy (AFM)

AFM measurements were conducted using an IR-neaSCOPE+fs instrument manufactured by Attocube Systems AG, Germany. Tips with Pt/Ir coating (ARROW NCPt from Nano World) were used in tapping mode with a nominal cantilever resonance frequency of 285 kHz, nominal force constant of 42 N/m and a tapping amplitude of about 90 nm.

Energy-dispersive X-ray spectroscopy (EDS)

EDS measurements were performed using a TESCAN VEGA3 SEM equipped with a Bruker, XFlash 6-30 EDS detector. The measurements were carried out at an accelerating voltage of 10 kV and a working distance of 15 mm, optimized for elemental analysis and spatial resolution. Spectra were acquired from selected regions based on scanning electron microscope (SEM) image. Rectangular area scans were chosen rather than point measurements, allowing for improved signal-to-noise ratio and averaging over the targeted area. Samples were mounted on the conductive carbon tape to minimize charging effects. Silicon peaks from the substrate were considered during analysis and deconvolution of overlapping signals. Quantification of the spectra were done using standard ZAF correction in the Bruker software.

Spectroscopic ellipsometry (SE)

Spectroscopic ellipsometry measurements were performed at incidence angles of 65°, 70°, and 75° over the spectral range from 0.57 to 5 eV using a V-VASE ellipsometer (J.A. Woollam, Lincoln, NE, USA) and analyzed with the WASE32 software. To characterize the thickness of the native SiO_2 layer, reference measurements were carried out on Si wafers without PdS_2 coatings. The PdS_2 film was modeled as a homogeneous layer, with its optical constants described using a multiple-oscillator model (see Supplementary Information (SI) for detailed description of the model). Specifically, the model includes two three-parameter Gaussian oscillators to represent the main critical-point absorption at the edge of the visible spectrum and higher-energy interband transitions. In addition, a pole term was included to account for the dispersion of the real part of the dielectric function at higher energies. The experimental data were then best fitted by optimizing the PdS_2 layer thickness and the dispersion-model parameters. In a second modeling approach, the real and imaginary parts of the dielectric function of the PdS_2 layer were determined by independently fitting the ellipsometric data at each photon-energy point, without assuming a specific dispersion model, while keeping the layer thickness fixed to the optimal value obtained from the first approach. The dielectric function obtained in this way was used to determine the nature and value of the band gap and to perform critical-point analysis.

View Article Online
DOI: 10.1039/D6NR00537C

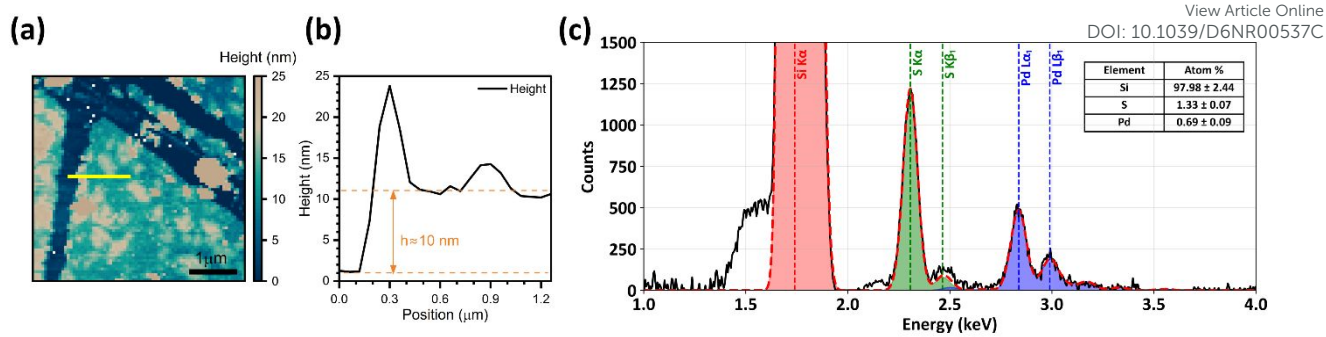

Fig. 2 (a) Topography image of the PdS_2 sample taken with AFM. The darker channel-like regions correspond to mechanically scratched areas exposing the underlying substrate. (b) Line height profile extracted along the yellow line shown in (a). (c) EDS spectrum with the subtracted background, along with the individual elemental peak components (Si, S, Pd).

Raman spectroscopy

Raman spectroscopy measurements were performed using a commercial Renishaw in-via Raman setup in a back-scattering geometry using a 532 nm laser for excitation. The incident beam polarization was rotated using a zero-order half-wave plate, and a vertical analyzer was placed before the detector to select the scattered polarization. The scattered light was collected through a microscope objective (magnification: 50×, numerical aperture: NA = 0.50) and directed into a spectrometer equipped with a 2400 gr/mm grating, providing a spectral resolution better than 1 cm^{-1}. All measurements were performed under ambient conditions with a laser power of 0.39 mW on the sample and an acquisition time of 5x1s per spectrum.

Second-harmonic generation (SHG) microscopy

The nonlinear SHG measurements were conducted with a custom-built scanning confocal optical microscope in a back-scattered geometry. The fundamental beam (1044 nm, 200 fs, 80 MHz) was linearly polarized and focused by a microscopic objective (50x long working distance objective lens; numerical aperture, NA=0.50) to the spot size of about 1.2 µm in diameter onto the sample at normal incidence. The average power at the sample surface was maintained at 12 mW. The reflected nonlinear optical signal was collected with the same objective. After passing through a dichroic beam splitter and band-pass filter, the fundamental beam was filtered out, and the nonlinear optical signal was detected by a fiber-coupled spectrograph equipped with a thermoelectrically cooled silicon electron multiplying charge-coupled device (EMCCD). To measure the incident laser polarization angle dependence of the nonlinear optical signal, we rotated the polarization of the fundamental beam with respect to the sample surface normal using an achromatic half-wave plate while the analyzer was kept at the fixed position.

Ultrafast differential reflectance (DR)

For time-resolved DR, a femtosecond laser system (Light Conversion Pharos), operating at 1 kHz, was used to pump a Light Conversion Orpheus optical parametric amplifier, generating pump pulses at 440 nm. The pump pulses were mechanically chopped at 500 Hz frequency (Thorlabs MC2000B). A small fraction of the fundamental beam at 1030 nm was focused on the sapphire plate to produce broadband supercontinuum stretching from 530 nm to 940 nm and used as a probe pulse. The probe pulse was directed through a motorized delay stage (Newport DL325), providing pump-probe delays of up to 1.8 ns. Using all reflective optics, both beams were focused onto the sample to approximately a 200 µm spot size for the pump beam and a 50 µm spot size for the probe beam, with the two beams having perpendicular polarizations. The overall temporal resolution of the DR setup was 70 fs. The details of the home-built transient absorption spectrometer can be found in the following publication.[31]

Results and discussion

Structural and optical characterization

To determine the sample thickness and overall morphology, AFM was employed. The AFM line profile shown in Fig. 2b, taken along the yellow line indicated in Fig. 2a, reveals a typical PdS_2 thickness of approximately 10 nm. The height was measured relative to a mechanically scratched region, where the PdS_2 film was removed to expose the underlying substrate. These exposed substrate regions appear as darker channel-like areas in Fig. 2a. The film, however, is not laterally uniform in thickness. This nonuniformity is more clearly visible in the higher-resolution scan of a smaller area shown in Fig. S1 in the SI, where sub-micron-sized islands with increased height are observed.

The background-subtracted EDS spectrum is shown in Fig. 2c, with spectral peaks fitted during quantification using the Esprit software and the P/B ZAF correction method. Spectra collected from multiple regions of the sample consistently yield a Pd:S ratio close to 1:2 within experimental uncertainty, confirming the stoichiometry of PdS_2. The inset table summarizes the atomic fractions together with the corresponding 1σ errors provided by the EDS software.

To determine the linear optical response of the PdS_2, we used SE. Fig. 3a shows the real and imaginary components of the resulting dielectric function, and Fig. 3b presents the corresponding refractive index and extinction coefficient. The experimental ellipsometry spectra and fitting results are shown

View Article Online
DOI: 10.1039/D6NR00537C

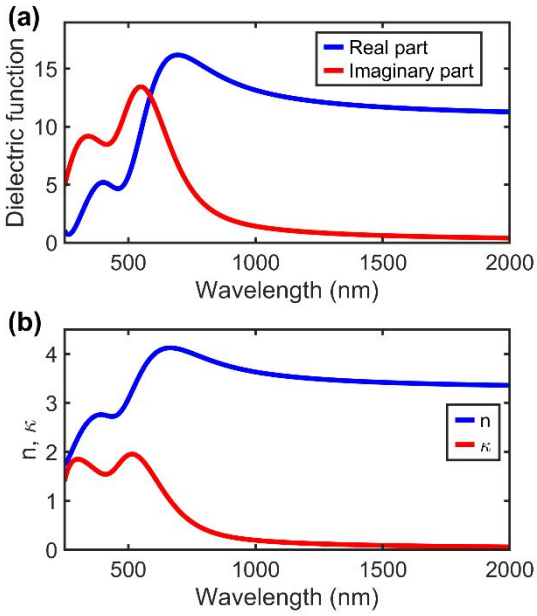

Fig. 3 Spectroscopic ellipsometry measurements showing (a) the dielectric function and (b) the refractive index and extinction coefficient of PdS_2 layer.

in Fig. S2 and Table S1. From the ellipsometric analysis, an effective PdS_2 layer thickness of 7.56 nm was extracted. The difference between this value and the thickness obtained from AFM measurements can be attributed to a combination of lateral thickness variations, partial film coverage, and uncertainties inherent to ellipsometric modeling, particularly for thin layered materials where surface roughness and optical anisotropy can influence the extracted thickness.

A pronounced absorption feature, manifested as a peak in the imaginary part of the dielectric function and in the extinction coefficient, dominates the optical absorption in the visible spectral range. To elucidate its physical origin, a critical-point analysis[32] was performed using the point-by-point extracted dielectric function. The results of the fitting procedure, presented in the Fig. S3 and Table S2, show that an excitonic lineshape model, with a critical-point energy at 2.08 eV, provides the best agreement with the experimental data. Similar resonant features at comparable energies have been reported for the closely related $PdSe_2$, where the excitonic nature is well established.[27,30,33] Available calculations for bulk 2O-PdS_2 consistently describe it as an indirect-gap semiconductor, with the first strong direct optical transition occurring at an energy higher than the indirect onset.[6,34,35] This qualitative picture is consistent with our experimental results, as the 2.08 eV resonance identified by critical-point analysis is assigned to a higher-energy direct optical transition with excitonic character, while the Tauc analysis of the point-by-point dielectric function yields an optical gap of 1.25 eV (Fig. S4), assigned to the onset of indirect transitions in the multilayer film. In addition to this dominant lower-energy feature, a higher-energy feature is also observed in the dielectric response. Since detailed calculations are not available for PdS_2 films with a thickness comparable to our sample, and since the available bulk literature does not provide a specific assignment beyond the indirect onset and the first strong direct transition, we assign this higher-energy structure more generally to higher-lying interband transitions.

The Raman spectrum of multilayer PdS_2 on a Si substrate, together with the corresponding (vibrational) mode assignments, is presented in Fig. 4. The measured Raman spectrum shows five characteristic peaks of bulk 2O-PdS_2, corresponding to the six modes accessible in back-scattering geometry. These peaks are assigned to: an overlapping A_g^1 and B_{1g}^1 modes (~245 cm^{-1}), followed by A_g^2 mode (~362 cm^{-1}), B_{1g}^2 mode (~384 cm^{-1}), A_g^3 mode (~464 cm^{-1}), and B_{1g}^3 mode (~482 cm^{-1}). To obtain the modes' frequency, full width at half maximum (FWHM) and intensity, we fitted the spectrum to a sum of multiple Lorentzian functions and listed all those parameters with corresponding uncertainties in Table S3. The spectrum matches previously reported experimental[8] and theoretical[6] results for PdS_2. It also closely resembles that of isostructural $PdSe_2$,[33,36–42] with all modes blue-shifted due to the lighter mass of sulfur.[8]

Beyond the expected bulk modes, an additional mode was observed at ~158 cm^{-1}. It resembles a mode that is symmetry-forbidden in bulk but becomes active in multilayer samples due to symmetry reduction. The same phenomenon was previously observed and explained in $PdSe_2$. [33,36–37,39–42] The presence of this mode proves that Raman spectroscopy is sensitive to layer-dependent symmetry breaking, even in relatively thick samples, consistent with earlier findings in $PdSe_2$.[33,37,41]

To further confirm the modes' symmetries, we performed polarization-dependent Raman measurements. Examples of polar plots for several vibrational modes are shown in Fig. 5, while the full set is provided in the SI (Fig. S5 and Fig. S6). The intensities of two modes (~384 cm^{-1} and ~482 cm^{-1}) remained unchanged, indicating B symmetry. All other modes displayed twofold symmetry, meaning they belong to a pure A or mixed A-B symmetry. Furthermore, the mode at 245 cm^{-1} shows a pronounced polarization-dependent frequency shift, increasing by ~2 cm^{-1} in the cross-polarized compared to the parallel-

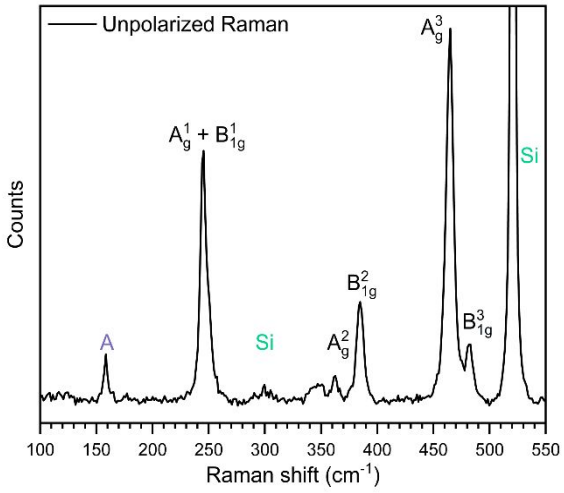

Fig. 4 Raman spectrum of multilayer PdS_2 on Si substrate. Bulk PdS_2 vibrational modes are labeled in black, vibrational mode activated due to symmetry reduction in violet, and silicon substrate modes in green.

View Article Online
DOI: 10.1039/D5NR00577G

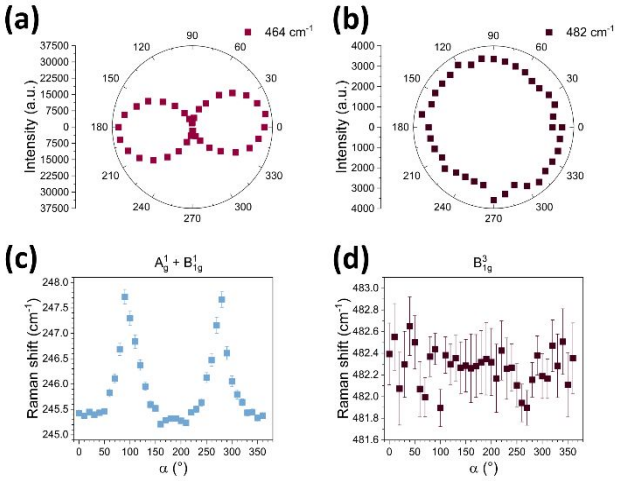

Fig. 5 (a,b) Polarization dependent intensity of vibrational modes, showing a A-mode signature with a two-lobe pattern (a) and an B-mode signature with angle-independent intensity (b). (c,d) Vibrational mode frequencies as a function of polarization angle. Panel (c) shows angular modulation that resolves two nearby frequencies with distinct polarization behavior, consistent with overlapped A and B modes, while (d) shows a constant frequency, indicating a pure mode.

polarized configuration. This behavior confirmed its assignment to overlapping A_g^1 and B_{1g}^1 vibrational modes.

Vibrational modes at 520 cm^{-1} and 300 cm^{-1} originate from the substrate.[43–45] It is worth noting that several earlier reports inadvertently assigned Si vibrational modes around 300 cm^{-1} and 420 cm^{-1} to PdS_2; a detailed discussion of this issue, together with Fig. S7 showing Si Raman spectrum, is provided in the SI. Based on our results, we rule out the presence of the 1T phase,[6] partially sulfurized Pd film (PdS),[46] and elemental sulfur.[47] The observed Raman-active phonon modes are not only fingerprints of symmetry, structure and purity, but also play a role in modulating ultrafast dynamics, as discussed later.

As previously mentioned, multilayer PdS_2 has a symmetry different from its bulk counterpart. Even-layered PdS_2 lacks inversion symmetry and belongs to the C_{2v} (mm2) point group,[48] enabling SHG. Because our sample contains regions with varying number of layers (Fig. 2a), we used SHG microscopy to locate an area with non-vanishing SHG response. The presence of SHG is consistent with theoretical expectations based on the crystal structure, and with previous reports on $PdSe_2$,[42] further confirming that our PdS_2 sample crystallizes in the 2O phase.

Polarization-resolved SHG (P-SHG) plots shown in Fig. 6, together with representative symmetry-allowed intensity patterns for the C_{2v} (mm2) point group,[49–51] of the even layered 2O PdS_2, illustrate qualitative consistency with the expected

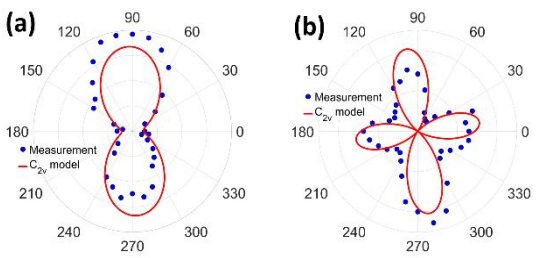

Fig. 6 P-SHG polar plots measured with a fixed analyzer aligned (a) parallel and (b) perpendicular to the laboratory X-axis while rotating the incident polarization. The points show the measured SHG intensity, while the solid red line represents representative symmetry-allowed intensity patterns for the C_{2v} (mm2) point group.[50]

symmetry behavior. The shapes of the polar plots are governed by the relative magnitudes of the susceptibility tensor elements and the angular orientation of the zigzag (ZZ) crystal directions. Variations in the P-SHG polar plot shapes reflect the anisotropy of the orthorhombic PdS_2. Furthermore, the observed SHG response demonstrates that PdS_2 remains sensitive to layer-dependent symmetry breaking, even in the multilayer sample.

Ultrafast Dynamics and Coherent Phonon Generation

Ultrafast pump-probe spectroscopy in reflection geometry was used to investigate the photoinduced reflectance response of PdS_2 under 440 nm pump pulse excitation. Since pump photon energy significantly exceeds the material's bandgap, electrons are efficiently excited from the valence band to the conduction band, generating a hot electron-hole plasma. Following pump excitation, a nonthermal carrier distribution relaxes toward a thermalized state through carrier–carrier and carrier–phonon scattering, followed by carrier cooling toward the band-edge extrema.[52]

The early-time (below 5 ps) DR map of PdS_2 is shown in Fig. 7a, along with selected spectral slices at various probe pulse delays (Fig. 7b), and time traces (Fig. 7c and 7d) at specific probe wavelengths. The photoinduced response features a broad positive DR change ($\Delta R/R > 0$) spanning ~580–930 nm at early delays, with a weaker negative signal ($\Delta R/R < 0$) at shorter wavelengths. The broad positive DR signal is consistent with a pump-induced modulation of the absorption coefficient, where an increase in absorption over this spectral region can produce a positive differential reflectance response.[53–55] Similar pump-induced increases in absorption over a comparable spectral region have been reported previously in $PdSe_2$, supporting this assignment.[27,30,53] The negative $\Delta R/R$ signal observed at shorter wavelengths spectrally overlaps with the pronounced absorption peak of PdS_2 (Fig. 3) suggesting its origin in bleaching of optical transitions associated with the absorption peak.

Early-time dynamics include a two-stage decay accompanied by a spectral blueshift, with zero-crossing wavelength shifting from ~580 nm initially to ~550 nm at later times. To describe the spectral evolution and quantify the early-time dynamics we used a global analysis procedure using Glotaran software.[56] The data are well described by a three-compartment sequential model, with the corresponding fitting results shown in Fig. S8. Applying the same model at additional pump fluences gives qualitatively similar behavior, again resolving the same two-step early-time dynamics (Fig. S9). The first two time constants extracted from the global fit, 370 ±7 fs and 1.143 ± 0.009 ps, account for the rapid evolution of both amplitude and spectral shape observed immediately after excitation. The third component corresponds to the spectral response of cold carriers, characterized by a nearly constant spectral shape with a decaying amplitude, whose amplitude dynamics will be discussed below. In the global analysis, this component was assigned an effectively infinite lifetime in order to separate the long-lived carrier population from the ultrafast spectral evolution at early delays. The associated spectra of all compartments exhibit a progressive shift of their maxima

View Article Online
DOI: 10.1039/D6NR00537C

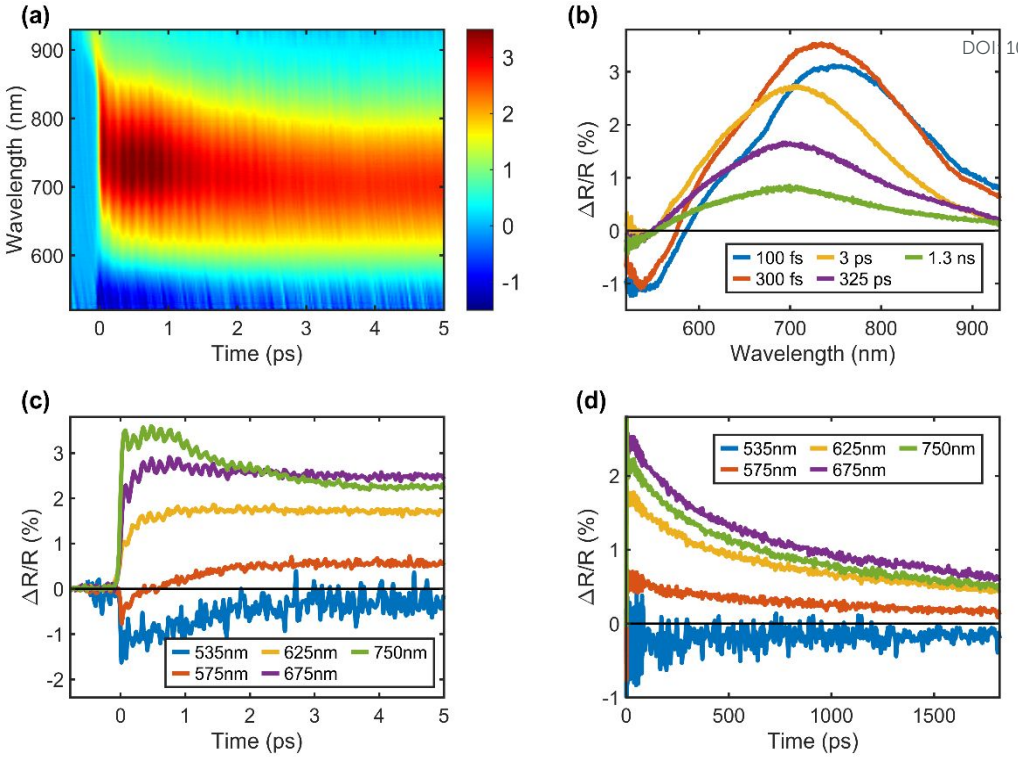

Fig. 7 (a) Early-time differential reflectance map of PdS_2, excited with 440 nm pump pulses at 1.3 mJ/cm² fluence and probed with white light supercontinuum. (b) Selected spectral traces. (c) Time traces up to 5 ps. (d) Time traces up to 1.8 ns.

toward shorter wavelengths, as shown in Fig. S8a. As seen in similar materials, BGR effect takes place upon ultrafast pump absorption due to enhanced screening of the Coulomb potential caused by photoinduced carriers and reduces the effective bandgap.[27,28,30] Following the initial BGR induced by carrier screening, the subsequent reduction of screening within the first few picoseconds,[28,57] leads to recovery of the bandgap and a blueshift of the absorption edge.[58] At the same time, carrier cooling and redistribution toward the band extrema result in state filling near the band edge, further modifying the effective absorption. Owing to the steep absorption profile in this spectral region, these changes produce large variations in the absorption coefficient and, consequently, in both the imaginary and real parts of the refractive index via the Kramers–Kronig relations, giving rise to the observed DR response. To further examine whether pump-induced modification of the equilibrium optical transition can account for the positive transient response, we performed a simple model calculation based on the dielectric function extracted from ellipsometry, in which the equilibrium dielectric response was shifted, the corresponding real part was recalculated via the Kramers–Kronig relation, and the optical response of the air/PdS_2/SiO_2/Si stack was evaluated using a transfer-matrix formalism (Fig. S10). The calculation qualitatively reproduces the measured positive transient signal, supporting the interpretation that the broad positive DR response originates from a pump-induced modification of the equilibrium optical transition, such as the BGR-driven shift discussed above. This shift changes the imaginary part of the dielectric function in the probed spectral region and therefore gives rise to a pump-induced increase in absorption.

Besides the spectral evolution, a reduction in the transient amplitude on sub-picosecond to picosecond timescales has been attributed in similar materials to carrier cooling[25,28,30,59] and to defect-assisted carrier capture.[26,29,59] Given that defects are common in CVD-grown TMDs,[60,61] a trapping contribution is likely present in our sample. In DR response, carrier cooling, BGR recovery, trapping, and band-edge filling act concurrently, so the observed spectral evolution and amplitude change reflects the time-dependent balance of these effects.

The recovery dynamics of the photoinduced response at later times (above 5 ps), corresponding to cold carriers, can be described with two decay constants, obtained by single-wavelength fitting (see Fig. S11), yielding average decay times of 240 ± 30 ps and 2.0 ± 0.1 ns, largely independent on the probe wavelength. A moderate increase in decay time is observed only for probe wavelengths longer than 800 nm indicating that this spectral region is more sensitive to a different population of states, likely closer to the band edge, which relax more slowly. Repeating the same fitting procedure for different pump fluences yields decay constants that remain unchanged within experimental uncertainty (Fig. S12), indicating no significant fluence dependence of the long-lived relaxation dynamics in the investigated fluence range. The two decay constants reflect contributions from multiple recombination pathways, such as intrinsic recombination and lattice-mediated processes,[25,53,62] as well as defect- or surface-assisted recombination.[26,27,54] Their exact origins, however, remain uncertain. In the noble-metal TMD family, reported decay constants span from tens of

View Article Online
DOI: 10.1039/D6NR00537C

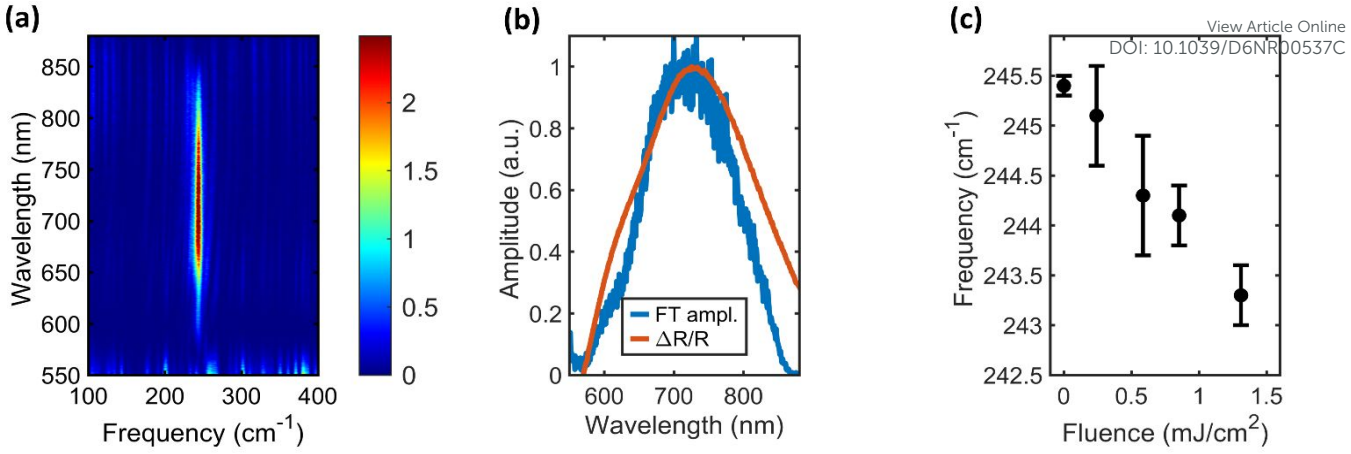

Fig. 8 (a) FT map of the fast-oscillating optical phonon component of the differential reflectance signal. (b) FT spectra (blue) extracted from (a), showing the phonon mode and its amplitude dependence on probe wavelength, together with the differential reflectance spectra (orange) averaged between 0 and 1.5 ps for comparison. (c) Pump-fluence dependence of phonon amplitude and frequency. The left axis shows the amplitude at 700 nm, and the right axis shows the phonon frequency, revealing mode softening with increasing excitation density. The first point at zero fluence is derived from polarization-resolved Raman spectroscopy, corresponding to mode A_g^1 only, rather than an overlapping A_g^1 and B_{1g}^1 peak.

picoseconds to several nanoseconds, depending on material, layer thickness, synthesis method, and sample quality.[25–27,53,54,62]

In the early-time response shown in Fig. 7a and 7c, a fast oscillatory modulation is evident. It originates from the generation of optical CPs through ultrafast pump excitation.[53,63,64] Two principal mechanisms underlie the generation of such CPs: impulsive stimulated Raman scattering (ISRS)[65] and displacive excitation of coherent phonons (DECP).[66] In strongly absorbing materials like PdS_2 and with above-bandgap photoexcitation conditions, DECP mechanism is expected to dominate.[64] Here, ultrafast carrier excitation causes a sudden shift in the lattice potential, displacing atoms from equilibrium and initiating a collective vibrational motion described by cosine-like oscillations. This mechanism predominantly excites totally symmetric Raman-active modes.[63,64,67–69] In our measurements, a dominant oscillatory mode with a frequency of 243.7 cm^{-1} (period of 136.8 fs) is extracted via Fourier transform (FT) of the DR signal (Fig. 8a). This mode is consistent with the measured A_g^1 symmetric vibrational mode (Fig. 4). The amplitude of the A_g^1 CP modulation, exhibits a wavelength dependence that closely follows the shape of the positive DR signal (Fig. 8b). Since the DR response is consistent with a pump-induced shift of the dielectric response, the spectral profile of the CP amplitude suggests that the CP response reflects a similar shift-like modulation of the same dielectric feature.[30,67,70] Due to the short oscillation period being comparable with our IRF and the oscillatory signal being superimposed with the nonoscillatory signal, the fitting procedure does not result in accurate determination of oscillation phase to verify the generation mechanism. With increasing fluence, and consequently a higher density of excited charge carriers, a shift in the phonon mode frequency is observed, as shown in Fig. 8c. The trend of the frequency shift in the DR measurements aligns with the steady-state Raman measurement at zero fluence, providing additional validation. Mode softening under photoexcitation is of electronic origin, as suggested by prior reports on TMDs, where similar behavior was attributed to transient carrier populations and deformation potential coupling effects.[71–74] Notably, phonon frequency renormalization is a time-dependent process,[73] with an initial, fast electronic softening followed by slower thermal contributions. Because the CP oscillations in our experiments decay rapidly and the analysis employs a full time-

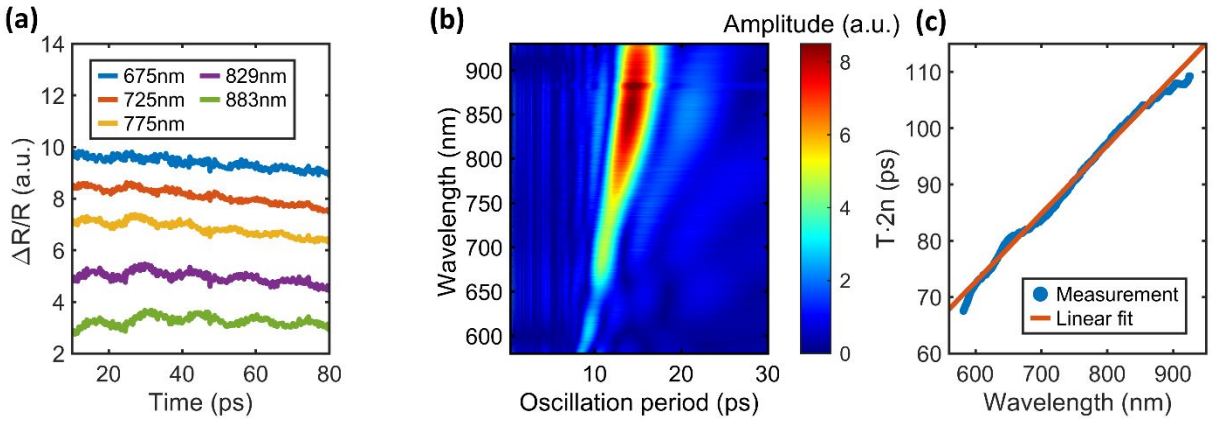

Fig. 9 Oscillatory signal corresponding to the CLAP mode measured at a pump fluence of 2.6 mJ/cm². (a) Zoomed-in differential reflectance traces for selected probe wavelengths, showing the oscillatory component of the transient signal. Traces are vertically shifted for clarity. (b) FT map of the oscillatory signal. (c) Linear relation between $2nT$ and probe wavelength λ. The solid red line represents a linear fit, and the inverse slope gives the longitudinal sound velocity in Si.

DOI: 10.1039/D6NR00557C

window FT, the measured shift represents a time-averaged value that primarily reflects the electronic component, while the slower thermal effects contribute less within the observed time window.

In addition to the optical CP discussed above, our measurements reveal a weak, low-frequency oscillation in the DR signal, most clearly visible at the highest pump fluence of 2.6 mJ/cm^2 (Fig. 9a). The oscillation period varies linearly with probe wavelength (Fig. 9c), indicative of traveling coherent longitudinal acoustic phonons (CLAPs).[75,76] Upon interaction with the sample, the pump pulses generate a traveling strain wave that modifies the local refractive index as it propagates through the PdS_2, and the underlying substrate. These strain waves are launched via two main mechanisms: either through thermally induced expansion of the unit cell or through the deformation potential resulting from the photoinduced charge carrier population. The probe pulse partially reflects off the propagating strain front and interferes with the beam reflected from fixed interfaces between the material layers. This interference results in the observed oscillatory signal in the DR traces. The dependence of the oscillation period on the probe wavelength is given by

$$T = \lambda/2nv, \quad (1)$$

where n is the refractive index of the medium (Si) and v is the corresponding acoustic velocity. From the measurements and linear fitting presented in Fig. 9c, we determined the acoustic velocity in Si to be v = 8250 ± 60 m/s, which agrees well with reported values.[75,77] Notably, no observable CLAP signal is found in our measurements of bare Si under similar measurement conditions, suggesting that PdS_2 acts as an efficient optoacoustic transducer in this layered structure. In the typical experiments involving semiconductive materials such as Si, CLAP generation often requires auxiliary optoacoustic transducers, realized with thin metal films or quantum wells deposited on the surface.[75,78]

Conclusions

In summary, we have conducted a comprehensive structural and optical characterization of multilayer PdS_2. Correlative structural analyses confirmed sample homogeneity and established an average film thickness of approximately 10 nm. Spectroscopic ellipsometry yielded the complex dielectric function, from which an indirect bandgap of 1.25 eV was determined. Nonlinear polarization resolved SHG microscopy and Raman spectroscopy verified the orthorhombic 2O phase. Ultrafast differential reflectivity measurements revealed complex transient dynamics, characterized by two fast components (370 fs and 1.143 ps) associated with early-time spectral evolution and carrier cooling and trapping, followed by slower processes (240 ps and 2 ns) attributed to carrier recombination. Oscillatory modulations in the transient signal were identified as CPs: an A_g^1 optical mode likely generated via displacive excitation, and a lower-frequency acoustic contribution arising from strain waves in the silicon substrate, highlighting PdS_2 as an efficient optoacoustic transducer.

Collectively, these findings bridge a critical knowledge gap in PdS_2, establish its fundamental optical properties, and lay the groundwork for future experimental studies and technological applications.

Author contributions

V.B.: transient reflectance measurements, analysis, and writing of manuscript; A.S.: AFM, SHG and Raman measurements, and writing of manuscript; P.I: Raman measurements and writing of manuscript; J.S.P.: spectroscopic ellipsometry measurements; P.S.: EDS measurements; J.Z., Y.W., and P.Y.: synthesis of the multilayer PdS_2; N.V.: SHG measurement, writing of manuscript, conceptual design of experiment; S.V.: transient reflectance measurements, writing of manuscript, conceptual design of experiment, and project management. All authors have read and agreed to the published version of the manuscript.

Conflicts of interest

There are no conflicts to declare.

Data availability

The supporting data has been provided as part of the Supplementary information. Additional data supporting this study are available from the corresponding author upon reasonable request.

Acknowledgements

This research was supported by the Environmental Protection and Energy Efficiency Fund of Republic of Croatia through public tender for development and innovation projects related to implementation of European Green Deal (ZO/ENU-1/22). This work was supported by the project Centre for Advanced Laser Techniques (CALT), co-funded by the European Union through the European Regional Development Fund under the Competitiveness and Cohesion Operational Programme (Grant No. KK.01.1.1.05.0001) and the project “Podizanje znanstvene izvrsnosti Centra za napredne laserske tehnike (CALTboost),” financed by the European Union through the National Recovery and Resilience Plan 2021–2026 (NRPP), A.S., P.I. and N.V. gratefully acknowledge Prof. Dr. Bojan Resan and Dr. Dario Novoselović for providing equipment (a femtosecond oscillator for the SHG setup) through a collaboration agreement between the Agricultural Institute in Osijek and the Institute of Physics. N.V. acknowledges financial support from the European Regional Development Fund for the project 'Materials for clean energy, advanced sensors and quantum technologies' (Grant No.PK.1.1.10.0002).

References

1 K. F. Mak and J. Shan, Photonics and optoelectronics of 2D semiconductor transition metal dichalcogenides, *Nat. Photonics*, 2016, **10**, 216–226.
2 H. Zeng and X. Cui, An optical spectroscopic study on two-dimensional group-VI transition metal dichalcogenides, *Chem. Soc. Rev.*, 2015, **44**, 2629–2642.
3 Y. Liu, N. O. Weiss, X. Duan, H.-C. Cheng, Y. Huang and X. Duan, Van der Waals heterostructures and devices, *Nat. Rev. Mater.*, 2016, **1**, 16042, DOI: 10.1038/natrevmats.2016.42.
4 T. Mueller and E. Malic, Exciton physics and device application of two-dimensional transition metal dichalcogenide semiconductors, *npj 2D Mater. Appl.*, 2018, **2**, 19, DOI: 10.1038/s41699-018-0074-2.
5 L. Huang, A. Krasnok, A. Alú, Y. Yu, D. Neshev and A. E. Miroshnichenko, Enhanced light–matter interaction in two-dimensional transition metal dichalcogenides, *Rep. Prog. Phys.*, 2021, **85**, 046401, DOI: 10.1088/1361-6633/ac45f9.
6 R. Kempt, A. Kuc and T. Heine, Two-dimensional noble-metal chalcogenides and phosphochalcogenides, *Angew. Chem. Int. Ed.*, 2020, **59**, 9242–9254.
7 J. H. Kim, H. Sung and G.-H. Lee, Phase engineering of two-dimensional transition metal dichalcogenides, *Small Sci.*, 2023, **4**, 2300093, DOI: 10.1002/smsc.202300093.
8 M. A. ElGhazali, P. G. Naumov, Q. Mu, V. Süß, A. O. Baskakov, C. Felser and S. A. Medvedev, Pressure-induced metallization, transition to the pyrite-type structure, and superconductivity in palladium disulfide PdS_2, *Phys. Rev. B*, 2019, **100,** 014507, DOI: 10.1103/physrevb.100.014507.
9 L.-Y. Feng, R. A. B. Villaos, Z.-Q. Huang, C.-H. Hsu and F.-C. Chuang, Layer-dependent band engineering of Pd dichalcogenides: a first-principles study, *New J. Phys.*, 2020, **22**, 053010, DOI: 10.1088/1367-2630/ab7d7a.
10 Y. Wang, Y. Li and Z. Chen, Not your familiar two dimensional transition metal disulfide: structural and electronic properties of the PdS_2 monolayer, *J. Mater. Chem. C*, 2015, **3**, 9603–9608.
11 S. Deng, L. Li and Y. Zhang, Strain modulated electronic, mechanical, and optical properties of the monolayer PdS_2, $PdSe_2$, and $PtSe_2$ for tunable devices, *ACS Appl. Nano Mater.*, 2018, **1**, 1932–1939.
12 Y.-S. Lan, X.-R. Chen, C.-E. Hu, Y. Cheng and Q.-F. Chen, Penta-PdX_2 (X = S, Se, Te) monolayers: promising anisotropic thermoelectric materials, *J. Mater. Chem. A*, 2019, **7**, 11134–11142.
13 M. Sharma, S. Nag, R. Kumar and R. Singh, Defect-induced modifications in electronic and thermoelectric properties of pentagonal PdX_2 (X = Se, S) monolayers, *Electron. Struct.*, 2024, **6**, 025007, DOI: 10.1088/2516-1075/ad46b8.
14 F. Hulliger, Electrical properties of some nickel-group chalcogenides, *J. Phys. Chem. Solids*, 1965, **26**, 639–645.
15 Y. Ma, X. Gong, F. Xiao, Y. Liu and X. Ming, First-principles study on the selective detection of toxic gases by 2D monolayer PdS_2: Insight into charge transfer dynamics and alignment of frontier molecular orbitals, *ACS Appl. Nano Mater.*, 2023, **6**, 12470–12478.
16 W. Zhang, Y. Cui, C. Zhu, B. Huang and S. Yan, Flexible ferroelasticity in monolayer PdS_2: a DFT study, *Phys. Chem. Chem. Phys.,* 2021, **23**, 10551–10559.
17 R. O. Figueiredo and L. Seixas, Hydrogen-evolution reaction in two-dimensional PdS_2 by phase and defect engineering, *Phys. Rev. Appl.*, 2022, **17**, 034035, DOI: 10.1103/physrevapplied.17.034035.
18 X. Zhang, G. Su, J. Lu, W. Yang, W. Zhuang, K. Han, X. Wang, Y. Wan, X. Yu and P. Yang, Centimeter-scale few-layer PdS_2: Fabrication and physical properties, *ACS Appl. Mater. Interfaces*, 2021, **13**, 43063–43074.
19 K. He, W. Xu, J. Tang, Y. Lu, C. Yi, B. Li, B. Li, H. Zhu, H. Zhang, X. Lin, Y. Feng, M. Zhu, J. Shen, M. Zhong, B. Li, B. Li and X. Duan, Centimeter-scale PdS_2 ultrathin films with high mobility and broadband photoresponse, *Small*, 2023, **19**, e2206915, DOI: 10.1002/smll.202206915.
20 C. Han, H. Chu, T. Feng, S. Zhao, D. Li, J. Zhao and W. Huang, Investigations on saturable absorption characteristic of PdS_2 and its application to high-peak-power sub-nanosecond intracavity OPO, *Opt. Mater.*, 2024, **154**, 115689, DOI: 10.1016/j.optmat.2024.115689.
21 P. K. Cheng, S. Liu, S. Ahmed, J. Qu, J. Qiao, Q. Wen and Y. H. Tsang, Ultrafast YB-doped fiber laser using few layers of PdS_2 saturable absorber, *Nanomaterials*, 2020, **10**, 2441, DOI: 10.3390/nano10122441.
22 P. K. Cheng, C. Y. Tang, X. Y. Wang, L.-H. Zeng and Y. H. Tsang, Passively Q-switched and femtosecond mode-locked erbium-doped fiber laser based on a 2D palladium disulfide (PdS_2) saturable absorber, *Photonics Res.*, 2020, **8**, 511, DOI: 10.1364/PRJ.380146.
23 R. Zhang, H. Mao, Z. Wang, S. Ma, S. Wu, Q. Wu, D. Liu, H. Li, Y. Fu, X. Li and T. Ma, In situ generated sulfate-facilitated efficient nitrate electrosynthesis on 2D PdS_2 with unique imitating growth feature, *Nano-Micro Lett.*, 2025, **17**, 289, DOI: 10.1007/s40820-025-01803-3.
24 A. Guha, R. Sharma, K. R. Sahoo, A. B. Puthirath, N. Shyaga, P. M. Ajayan and T. N. Narayanan, One-dimensional hollow structures of 2O-PdS_2 decorated carbon for water electrolysis, *ACS Appl. Energy Mater.*, 2021, **4**, 8715–8720.
25 D. Li, J. Fu, P. Suo, W. Zhang, B. Lu, X. Lin, X. Yan, B. Li, G. Ma and J. Yao, Layer dependent interlayer coherent phonon dynamics in $PdSe_2$ films, *Appl. Phys. Lett.*, 2021, **118**, 191105, DOI: 10.1063/5.0050475.
26 X. Chen, J. Huang, C. Chen, M. Chen, G. Hu, H. Wang, N. Dong and J. Wang, Broadband nonlinear photoresponse and ultrafast carrier dynamics of 2D $PdSe_2$, *Adv. Opt. Mater.*, 2022, **10**, 2101963, DOI: 10.1002/adom.202101963.
27 H. Chen, A. Kuklin, J. Xiao, O. A. Al-Hartomy, A. Al-Ghamdi, S. Wageh, Y. Zhang, H. Ågren, L. Gao and H. Zhang, Direct observation of photon induced giant band renormalization in 2D $PdSe_2$ dichalcogenide by transient absorption spectroscopy, *Small*, 2023, **19**, e2302760, DOI: 10.1002/smll.202302760.
28 G. Wang, K. Wang, N. McEvoy, Z. Bai, C. P. Cullen, C. N. Murphy, J. B. McManus, J. J. Magan, C. M. Smith, G. S. Duesberg, I. Kaminer, J. Wang and W. J. Blau, Ultrafast carrier dynamics and bandgap renormalization in layered $PtSe_2$, *Small*, 2019, **15**, e1902728, DOI: 10.1002/smll.201902728
29 H. J. Shin, S. Bae and S. Sim, Ultrafast Auger process in few-layer $PtSe_2$, *Nanoscale*, 2020, **12**, 22185–22191.
30 Z. Li, B. Peng, M.-L. Lin, Y.-C. Leng, B. Zhang, C. Pang, P.-H. Tan, B. Monserrat and F. Chen, Phonon-assisted electronic states modulation of few-layer $PdSe_2$ at terahertz frequencies, *npj 2D Mater. Appl.*, 2021, **5**, 87, DOI: 10.1038/s41699-021-00268-3.
31 V. Brusar, M. Forjan, I. Ljubić, M. Alešković, K. Becker and S. Vdović, Ultrafast photoelimination of nitrogen from upper excited states of diazoalkanes and the fate of carbenes formed in the reaction, *J. Org. Chem.*, 2023, **88**, 4286–4300.
32 P. Lautenschlager, M. Garriga, L. Viña and M. Cardona, Temperature dependence of the dielectric function and interband critical points in silicon, *Phys. Rev. B*, 1987, **36**, 4821–4830.
33 M. Wei, J. Lian, Y. Zhang, C. Wang, Y. Wang and Z. Xu, Layer-dependent optical and dielectric properties of centimeter-scale $PdSe_2$ films grown by chemical vapor deposition, *npj 2D Mater. Appl.*, 2022, **6**, 1, DOI:10.1038/s41699-021-00282-5.
34 W. Lei, W. Wang, X. Ming, S. Zhang, G. Tang, X. Zheng, H. Li and C. Autieri, Structural transition, metallization, and superconductivity in quasi-two-dimensional layered PdS_2 under compression, *Phys. Rev. B*, 2020, **101**, 205149, DOI: 10.1103/PhysRevB.101.205149.

35 S. Deng, M. Tao, J. Mei, M. Li, Y. Zhang and L. Li, Optical and piezoelectric properties of strained orthorhombic PdS_2, *IEEE Trans. Nanotechnol.*, 2019, **18**, 358–364.
36 A. D. Oyedele, S. Yang, L. Liang, A. A. Puretzky, K. Wang, J. Zhang, P. Yu, P. R. Pudasaini, A. W. Ghosh, Z. Liu, C. M. Rouleau, B. G. Sumpter, M. F. Chisholm, W. Zhou, P. D. Rack, D. B. Geohegan and K. Xiao, $PdSe_2$: Pentagonal two-dimensional layers with high air stability for electronics, *J. Am. Chem. Soc.*, 2017, **139**, 14090–14097.
37 W. L. Chow, P. Yu, F. Liu, J. Hong, X. Wang, Q. Zeng, C. Hsu, C. Zhu, J. Zhou, X. Wang, J. Xia, J. Yan, Y. Chen, D. Wu, T. Yu, Z. Shen, H. Lin, C. Jin, B. K. Tay and Z. Liu, High mobility 2D palladium diselenide field-effect transistors with tunable ambipolar characteristics, *Adv. Mater.*, 2017, **29**, 1602967, DOI: 10.1002/adma.201602969.
38 L. Chen, W. Zhang, H. Zhang, J. Chen, C. Tan, S. Yin, G. Li, Y. Zhang, P. Gong and L. Li, In-plane anisotropic thermal conductivity of low-symmetry $PdSe_2$, *Sustainability*, 2021, **13**, 4155, DOI: 10.3390/su13084155.
39 J. Yu, X. Kuang, Y. Gao, Y. Wang, K. Chen, Z. Ding, J. Liu, C. Cong, J. He, Z. Liu and Y. Liu, Direct observation of the linear dichroism transition in two-dimensional palladium diselenide, *Nano Lett.*, 2020, **20**, 1172–1182.
40 T. Das, D. Seo, J. E. Seo and J. Chang, Tunable current transport in $PdSe_2$ via layer-by-layer thickness modulation by mild plasma, *Adv. Electron. Mater.*, 2020, **6**, 202000008, DOI:10.1002/aelm.202000008.
41 A. A. Puretzky, A. D. Oyedele, K. Xiao, A. V. Haglund, B. G. Sumpter, D. Mandrus, D. B. Geohegan and L. Liang, Anomalous interlayer vibrations in strongly coupled layered $PdSe_2$, *2D Mater.*, 2018, **5**, 035016, DOI: 10.1088/2053-1583/aabe4d.
42 J. Yu, X. Kuang, J. Li, J. Zhong, C. Zeng, L. Cao, Z. Liu, Z. Zeng, Z. Luo, T. He, A. Pan and Y. Liu, Giant nonlinear optical activity in two-dimensional palladium diselenide, *Nat. Commun.*, 2021, **12**, 1083, DOI: 10.1038/s41467-021-21267-4.
43 P. A. Temple and C. E. Hathaway, Multiphonon raman spectrum of silicon, *Phys. Rev. B*, 1973, **7**, 3685–3697.
44 C. S. Wang, J. M. Chen, R. Becker and A. Zdetsis, Second order Raman spectrum and phonon density of states of silicon, *Phys. Lett. A*, 1973, **44**, 517–518.
45 W.-J. Lee and Y.-H. Chang, Growth without postannealing of monoclinic VO_2 thin film by atomic layer deposition using VCl_4 as precursor, *Coatings*, 2018, **8**, 431, DOI: 10.3390/coatings8120431.
46 L.-C. Chen, Z.-Y- Cao, H. Yu, B.-B. Jiang, L. Su, X. Shi, L.-D. Chen and X.J. Chen, Phonon anharmonicity in thermoelectric palladium sulfide by Raman spectroscopy, *Appl. Phys. Lett.,* 2018, **113**, 022105, DOI: 10.1063/1.5041973.
47 C. Nims, B. Cron, M. Wetherington, J. Macalady and J. Cosmidis, Low frequency Raman spectroscopy for micron-scale and in vivo characterization of elemental sulfur in microbial samples, *Sci. Rep.*, 2019, **9**, 7971, DOI: 10.1038/s41598-019-44353-6.
48 L. Pi, L. Li, K. Liu, Q. Zhang, H. Li and T. Zhai, Recent progress on 2D noble-transition-metal dichalcogenides, *Adv. Funct. Mater.,* 2019, **29**, 1904932, DOI: 10.1002/adfm.201904932.
49 G. M. Maragkakis, S. Psilodimitrakopoulos, L. Mouchliadis, A. S. Sarkar, A. Lemonis, G. Kioseoglou and E. Stratakis, Nonlinear optical imaging of in-plane anisotropy in two-dimensional SNS, *Adv. Opt. Mater.*, 2022, **10**, 2102776, DOI: 10.1002/adom.202102776.
50 C. He, H. Chao, R. Wu, S. Li, Q. Lei, X. Cao, Z. Cao, L. Zhu, H. Wang, Q. Zhao and X. Xu, Structural symmetry-breaking-driven giant optical second harmonic generation in Janus monolayer ReSSe, *J. Phys. Chem. C*, 2023, **127**, 14991–14998.
51 C. He, R. Wu, L. Zhu, Y. Huang, W. Du, M. Qi, Y. Zhou, Q. Zhao and X. Xu, Anisotropic second-harmonic generation induced by reduction of in-plane symmetry in 2D materials with strain engineering, *J. Phys. Chem. Lett.*, 2022, **13**, 352–361.
52 Z. Nie, R. Long, L. Sun, C.-C. Huang, J. Zhang, Q. Xiong, D. W. Hewak, Z. Shen, O. V. Prezhdo and Z.-H. Loh, Ultrafast carrier thermalization and cooling dynamics in few-layer MoS_2, *ACS Nano*, 2014, **8**, 10931–10940.
53 C.-F. Huo, R. Wen, X.-Q. Yan, D.-K. Li, K.-X. Huang, Y. Zhu, Q. Cui, C. Xu, Z.-B. Liu and J.-G. Tian, Thickness-dependent ultrafast charge-carrier dynamics and coherent acoustic phonon oscillations in mechanically exfoliated $PdSe_2$ flakes, *Phys. Chem. Chem. Phys.*, 2021, **23**, 20666–20674.
54 S. Jiang, J. Yang, L. Zhu, J. Xie, W. Guo, E. Zhao, C. Chen, T. Wang, F. Su, Y. Zhang and J. Lin, Nonlinear electronic and ultrafast optical signatures in chemical vapor-deposited ultrathin PtS_2 ribbons, *Nano Res.*, 2022, **15**, 4366–4373.
55 S. Jiang, J. Yang, Y. Shi, J. Zhao, C. Xie, L. Zhao, J. Fu, P. Yang, Y. Huan, Q. Xie, H. Jiang, Q. Zhang, X. Wang, F. Su and Y. Zhang, salt-assisted growth and ultrafast photocarrier dynamics of large-sized monolayer $ReSe_2$, *Nano Res.*, 2020, **13**, 667–675.
56 J. J. Snellenburg, S. P. Laptenok, R. Seger, K. M. Mullen and I. H. M. Van Stokkum, Glotaran: A Java-based graphical user interface for the R package TIMP, *J. Stat. Softw.*, 2012, **49**, 1-22.
57 O. Abdul-Aziz, M. Tuniz, W. Bronsch, F. Parmigiani, F. Cilento, D. Wolverson, C. J. Sayers, G. Cerullo, C. Dallera, E. Carpene, P. H. M. Van Loosdrecht and H. Hedayat, Photoinduced electronic band dynamics and defect-mediated surface potential evolution in $PdSe_2$, *npj 2D Mater. and Appl.*, 2025, **9**, 110, DOI: 10.1038/s41699-025-00629-2.
58 L. Tian, L. Di Mario, V. Zannier, D. Catone, S. Colonna, P. O'Keeffe, S. Turchini, N. Zema, S. Rubini and F. Martelli, Ultrafast carrier dynamics, band-gap renormalization, and optical properties of ZnSe nanowires, *Phys. Rev. B*, 2016, **94**, 165442, DOI: 10.1103/physrevb.94.165442.
59 X. Lyu, Y. Li, X. Li, X. Liu, J. Xiao, W. Xu, P. Jiang, H. Yang, C. Wu, X. Hu, L.-Y. Peng, Q. Gong, S. Yang and Y. Gao, Layer-dependent ultrafast carrier dynamics of $PdSe_2$ investigated by photoemission electron microscopy, *Nanoscale*, 2024, **16**, 9317–9324.
60 W. Zhou, X. Zou, S. Najmaei, Z. Liu, Y. Shi, J. Kong, J. Lou, P. M. Ajayan, B. I. Yakobson and J.-C. Idrobo, Intrinsic structural defects in monolayer molybdenum disulfide, *Nano Lett.*, 2013, **13**, 2615–2622.
61 M. F. Hossen, S. Shendokar and S. Aravamudhan, Defects and Defect engineering of two-dimensional transition metal dichalcogenide (2D TMDC) materials, *Nanomaterials*, 2024, **14**, 410, DOI: 10.3390/nano14050410.
62 G. Li, X. Zhang, Y. Wang, Z. Bai, H. Zhao, J. He and D. He, Ultrafast transient absorption measurements of photocarrier dynamics in $PdSe_2$, *Nanoscale*, 2023, **15**, 14994–14999.
63 T. Y. Jeong, B. M. Jin, S. H. Rhim, L. Debbichi, J. Park, Y. D. Jang, H. R. Lee, D.-H. Chae, D. Lee, Y.-H. Kim, S. Jung and K. J. Yee, Coherent lattice vibrations in mono- and few-Layer WSe_2, *ACS Nano*, 2016, **10**, 5560–5566.
64 Z. Li, Y. Chen, A. Song, J. Zhang, R. Zhang, Z. Zhang and X. Wang, Anisotropic phonon dynamics in Dirac semimetal $PtTe_2$ thin films enabled by helicity-dependent ultrafast light excitation, *Light Sci. Appl.*, 2024, **13**, 181, DOI: 10.1038/s41377-024-01540-z.
65 L. Dhar, J. A. Rogers and K. A. Nelson, Time-resolved vibrational spectroscopy in the impulsive limit, *Chem. Rev.*, 1994, **94**, 157–193.
66 H. J. Zeiger, J. Vidal, T. K. Cheng, E. P. Ippen, G. Dresselhaus and M. S. Dresselhaus, Theory for displacive excitation of coherent phonons, *Phys. Rev. B*, 1992, **45**, 768–778.
67 C. Trovatello, H. P. C. Miranda, A. Molina-Sánchez, R. Borrego-Varillas, C. Manzoni, L. Moretti, L. Ganzer, M. Maiuri, J. Wang, D. Dumcenco, A. Kis, L. Wirtz, A. Marini, G. Soavi, A. C. Ferrari,

View Article Online
DOI: 10.1039/D6NR00537C

G. Cerullo, D. Sangalli and S. D. Conte, Strongly coupled coherent phonons in single-layer MoS_2, *ACS Nano*, 2020, **14**, 5700–5710.

68 T. Fukuda, K. Makino, Y. Saito, P. Fons, A. Ando, T. Mori, R. Ishikawa, K. Ueno, J. Afalla and M. Hase, Coherent optical response driven by non-equilibrium electron–phonon dynamics in a layered transition-metal dichalcogenide, *APL Mater.*, 2024, **12**, 021102, DOI: 10.1063/5.0188537.

69 R. Wu, Y. Zhang, M. Shahjahan and E. Harel, Rapid wide-field correlative mapping of electronic and vibrational ultrafast dynamics in solids, *ACS Nano*, 2025, **19**, 7064–7074.

70 S. Mor, V. Gosetti, A. Molina-Sánchez, D. Sangalli, S. Achilli, V. F. Agekyan, P. Franceschini, C. Giannetti, L. Sangaletti and S. Pagliara, Photoinduced modulation of the excitonic resonance via coupling with coherent phonons in a layered semiconductor, *Phys. Rev. Res.*, 2021, **3**, 043175, DOI: 10.1103/PhysRevResearch.3.043175.

71 D. Soranzio, M. Savoini, P. Beaud, F. Cilento, L. Boie, J. Dössegger, V. Ovuka, S. Houver, M. Sander, S. Zerdane, E. Abreu, Y. Deng, R. Mankowsky, H. T. Lemke, F. Parmigiani, M. Peressi and S. L. Johnson, Strong modulation of carrier effective mass in WTe_2 via coherent lattice manipulation, *npj 2D Mater. Appl.*, 2022, **6**, 71, DOI: 10.1038/s41699-022-00347-z.

72 B. He, C. Zhang, W. Zhu, Y. Li, S. Liu, X. Zhu, X. Wu, X. Wang, H.-H. Wen and M. Xiao, Coherent optical phonon oscillation and possible electronic softening in WTe_2 crystals, *Sci. Rep.*, 2016, **6**, 30487, DOI: 10.1038/srep30487.

73 A. M. Finardi, C. Fasolato, A. Giugni, M. Capeccia, R. Cucini, E. Cappelluti, F. Sacchetti, G. Panaccione, P. Postorino, C. Petrillo and G. Rossi, Transient photodoping and phonon dynamics in bulk and monolayer MoS_2 by time resolved Raman scattering, *npj 2D Mat. Appl.*, 2025, **9**, 79, DOI: 10.1038/s41699-025-00601-0.

74 N. Girotto, F. Caruso and D. Novko, Ultrafast nonadiabatic phonon renormalization in photoexcited single-layer MoS_2, *J. Phys. Chem. C*, 2023, **127**, 16515–16524.

75 F. Vialla and N. Del Fatti, Time-domain investigations of coherent phonons in van der Waals thin films, *Nanomaterials*, 2020, **10**, 2543, DOI: 10.3390/nano10122543.

76 S. Ge, X. Liu, X. Qiao, Q. Wang, Z. Xu, J. Qiu, P.-H. Tan, J. Zhao and D. Sun, Coherent longitudinal acoustic phonon approaching THz frequency in multilayer molybdenum disulphide, *Sci. Rep.*, 2014, **4**, 5722, DOI: 10.1038/srep05722.

77 K. Ishioka, A. Rustagi, U. Höfer, H. Petek and C. J. Stanton, Intrinsic coherent acoustic phonons in the indirect band gap semiconductors Si and GaP, *Phys. Rev. B*, 2017, **95**, 035205, DOI: 10.1103/PhysRrevB.95.035205.

78 A. Devos and R. Côte, Strong oscillations detected by picosecond ultrasonics in silicon: evidence for an electronic-structure effect, *Phys. Rev. B*, 2004, **70**, 125208, DOI: 10.1103/PhysRrevB.70.125208.

View Article Online
DOI: 10.1039/D6NR00537C

The supporting data has been provided as part of the Supplementary information.

Additional data supporting this study are available from the corresponding author upon reasonable request.